Satellite Navigation
https://satellite-navigation.springeropen.com/

ORIGINAL ARTICLE

Open Access

Ionospheric gradient estimation using ground-based GEO observations for monitoring multi-scale ionospheric dynamics

Zhiyao Li[1,3], Jiahao Zhong[1,5], Ningbo Wang[2*], Yongqiang Hao[1], Xin Wan[1,5], N. Jakowski[4], M. M. Hoque[4], Ang Liu[2], Zishen Li[2,3], Runqing Liu[2] and Grzegorz Nykiel[4]

Abstract

High-resolution and real-time monitoring of ionospheric dynamics is important for space weather research and satellite-based communication and navigation. However, the existing observational frameworks often face trade-offs between spatial coverage, temporal continuity, and resolution. This study presents a novel fixed-geometry observation framework, which utilizes the ionospheric gradients derived from a network of Geostationary Earth Orbit (GEO) satellites and ground-based Global Navigation Satellite System (GNSS) receivers. The stationary geometry between GEO satellites and ground receivers enables the formation of dense, fixed Ionospheric Pierce Points (IPPs), and geometry-invariant inter-IPP baselines, which serve as fundamental sensing units. Leveraging this configuration, the proposed framework produces high-resolution ionospheric Total Electron Content (TEC) gradient fields (spatially < 0.25°, temporally 30 s), without requiring satellite motion corrections. This enables multi-scale analysis of ionospheric disturbances in real time. Case studies demonstrate the framework can resolve sub-minute electron density variations during the diurnal development of Equatorial Ionization Anomalies (EIA), track the evolution of plasma irregularities associated with Equatorial Plasma Bubbles (EPBs), and characterize the propagation of Large-scale Traveling Ionospheric Disturbances (LSTIDs). The GEO-based framework provides a geometry-consistent and scalable tool that bridges the gap between sparse satellite observations and high-resolution ionospheric diagnostics, which is significant for both scientific investigation and operational space weather monitoring.

Keywords Ionospheric dynamics, Geostationary earth orbit (GEO), Total electron content gradient, Fixed-geometry observation network

Introduction

Ionospheric dynamics are the sensitive indicators of the geospace state, reflecting the complex multi-scale coupling processes driven by solar-terrestrial interactions, geomagnetic field variations, and neutral atmospheric dynamics (Buonsanto, 1999; Francis, 1974; Hedin, 1987; Sheng et al., 2025). These processes elicit diverse responses, including rapid ionospheric fluctuations during geomagnetic storms (Gonzalez et al., 1994), disturbances induced by atmospheric gravity waves (Hocke & Schlegel, 1996), and the formation of Equatorial Plasma Bubbles (EPBs) in low-latitude regions (Tsunoda et al., 1982). Given the ionosphere's variability in multiple

*Correspondence:
Ningbo Wang
wangningbo@aoe.ac.cn
[1] Planetary Environmental and Astrobiological Research Laboratory (PEARL), School of Atmospheric Sciences, Sun Yat-Sen University, Zhuhai, China
[2] Aerospace Information Research Institute (AIR), Chinese Academy of Sciences (CAS), Beijing, China
[3] QiLu Aerospace Information Research Institute, Jinan, China
[4] Institute for Solar-Terrestrial Physics, German Aerospace Center (DLR), Neustrelitz, Germany
[5] Key Laboratory of Tropical Atmosphere-Ocean System, Ministry of Education, Zhuhai, China

spatial and temporal scales, high-resolution and real-time monitoring is essential for early warning of space-weather impacts on satellite-based communication and navigation systems (Carter et al., 2023; Tang et al., 2024). However, commonly used satellite-based platforms have inherent limitations. Satellite-based systems such as those in Medium Earth Orbit (MEO) and Low Earth Orbit (LEO) provide sparse temporal coverage in specific regions, while ground-based radars and airglow imagers are limited to regional coverage (Han et al., 2024; Zhong et al., 2019). To capture these coupling processes and their temporal evolution, a monitoring framework that provides high spatial resolution, continuous temporal coverage, and broad geographic extent is required.

The combination of Global Navigation Satellite System (GNSS) Geostationary Earth Orbit (GEO) satellites with ground-based receivers establishes a unique observational geometry for ionospheric monitoring. A GEO satellite is a geosynchronous satellite in the Earth's equatorial plane with near zero inclination and eccentricity, which means it remains fixed in the sky relative to an observer on Earth's surface (Wang et al., 2020; Yang et al., 2020). This stationary geometry enables continuous monitoring of Total Electron Content (TEC) along fixed Lines Of Sight (LOS), providing high temporal resolution ideal for capturing both gradual variability and sudden anomalies (Han et al., 2024; Huang et al., 2023). Previous studies used BeiDou Navigation Satellite System (BDS) GEO satellite data. For instance, GEO-based measurements were used to detect Traveling Ionospheric Disturbances (TIDs) and estimate the altitude and zonal drift velocity of ionospheric irregularities (Huang et al., 2025; Rao et al., 2025; Zhong et al., 2023). However, earlier studies were limited by sparse receiver distributions, which restricted spatial coverage and confined most analyses to the comparisons between a few Ionospheric Pierce Points (IPPs). Notably, the fixed-geometry of GEO-receiver LOS fundamentally differs from the moving-geometry of MEO-receiver paths, raising the question of whether this geometric stability can be more effectively leveraged. Recently, dense BDS-GEO receiver networks are deployed in low and mid-latitude East Asia (Yang et al., 2020). However, a dedicated framework that fully exploits this geometric advantage for dynamic ionospheric analysis is still needed.

The fixed-geometry observation network formed by ground-based GNSS receivers and GEO satellites establishes a dense and stable sensing architecture for monitoring ionospheric dynamics. With the receivers tracking the same GEO satellites, an array of stationary IPPs is formed, and the geometry of any vectors connecting two IPPs is invariant (Li et al., 2023). Each inter-IPP vector serves as an independent sensing unit, with the TEC difference along the vector functioning as its observable (Jakowski & Hoque, 2019). Mathematically, the number of inter-IPP vectors scales approximately up to $N(N-1)/2$ for N IPPs, enhancing both spatial resolution and measurement redundancy. By leveraging the geometric invariance of inter-IPP vectors, the horizontal TEC gradient vectors can be derived directly from the simultaneous TEC difference vectors for each vector, which is inherently free from motion-induced aliasing or elevation-angle corrections. Similarly, the temporal derivative of local TEC is derived from the time series at each stationary IPP (Jakowski et al., 2012). This configuration enables the concurrent estimation of spatial and temporal TEC gradients. Moreover, the availability of BDS-GEO satellites at multiple longitudes provides diverse viewing geometries.

In this work, we present a monitoring framework for ionospheric dynamics based on the BDS-GEO fixed-geometry observation network. The system consists of a dense array of stationary IPPs and a set of geometry-invariant vectors that inherently interconnect IPP pairs. First, we describe a methodology that treats each inter-IPP vector as a fundamental sensing unit for estimating both spatial and temporal TEC gradients. Then, we evaluate the framework using three representative case studies: (1) The diurnal evolution of the Equatorial Ionization Anomaly (EIA), (2) The evolution of electron density inhomogeneity induced by EPBs, and (3) The propagation characteristics of Large-scale TIDs (LSTIDs). Finally, we discuss the framework's diagnostic performance and broader applications.

The receiver network and set of GEO satellites

In this study, a network of 207 ground-based GNSS receivers and five GEO satellites from the BDS are utilized. Table 1 provides the detailed information about the five GEO satellites, including their Pseudo Random Noise (PRN), satellite name, longitude, launch date, and inclination. Figure 1 shows the geographical distribution of the receivers, which are predominantly concentrated in the middle and low latitudes with an average spacing of approximately 200 km.

Table 1 Lists of the GEO satellites used in this study

PRN	Satellite name	Longitude	Launch date	Inclination (°)
C01	BDS2 GEO8	144.5 °E	2019-05-17	0.4001
C02	BDS2 GEO6	84.0 °E	2012-10-25	1.4764
C03	BDS2 GEO7	110.5 °E	2016-06-12	1.5196
C04	BDS2 GEO4	160.0 °E	2010-10-31	0.8047
C05	BDS2 GEO5	59.0 °E	2012-02-24	1.8963

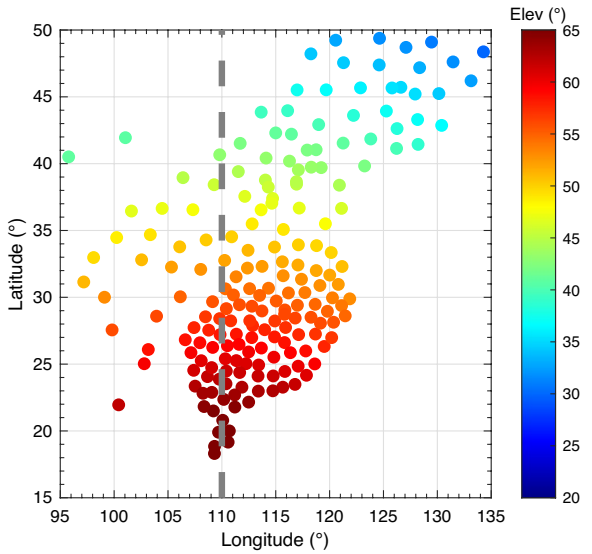

Fig. 1 The location of the receivers. The pseudo-color indicates the mean elevation angle of the LOS from the GEO satellite C03 to each receiver on 2024-09-21. The gray line marks the mean sub-satellite longitude of C03

Processing the TEC derived from GEO satellites

The estimation of ionospheric TEC gradients is based on the Slant TEC (STEC) derived from GEO satellites. The STEC utilized in this study is obtained from the dual-frequency carrier-phase observations, which can be described as:

$$T_S = \frac{{f_1}^2 {f_2}^2}{40.3({f_1}^2 - {f_2}^2)} [(\lambda_1 L_1 - \lambda_2 L_2) - (\lambda_1 N_1 - \lambda_2 N_2) + (d_1 - d_2)] \quad (1)$$

where T_S represents the STEC. L_1 and L_2 are carrier-phase measurements at two different frequencies f_1 and f_2, d_1 and d_2 are hardware biases at two frequencies f_1 and f_2, and $\lambda_1 N_1 - \lambda_2 N_2$ is the carrier-phase ambiguity. In this study, STEC is derived from the B1I–B3I dual-frequency carrier-phase measurements with elevation angles greater than 20°. Specifically, B1I and B3I correspond to carrier frequencies of 1561.098 MHz and 1268.52 MHz, with observation codes L2I and L6I of carrier-phase, respectively.

To obtain absolute STEC values, the ambiguity term is eliminated using the Carrier–Code Leveling (CCL) method (Mannucci et al., 1998). Satellite and receiver Differential Code Biases (DCBs) are corrected using the daily DCB product provided by the Chinese Academy of Sciences (CAS, Wang et al., 2016, 2026, https://data.bdsmart.cn/pub/product/bias/). After these corrections, the carrier-phase STEC is converted to absolute STEC. The STEC is then mapped to Vertical TEC (VTEC) using a mapping function. The mapping function $M(\delta)$ is defined under the single-layer ionospheric shell model (Klobuchar, 1987; Zhong et al., 2016a), assuming a fixed height of 400 km, and is defined as:

$$M(\delta) = \frac{1}{\sqrt{1 - \left(\frac{R_e \cos\delta}{R_e + h}\right)^2}} \quad (2)$$

where R_e is the Earth's radius, h is the shell height, and δ is the satellite elevation angle. Then, the relationship between absolute STEC and VTEC at IPP i can be described as:

$$T_S^i = M\left(\delta^i\right) \bullet T_V^i + b_{RDCB} + b_{SDCB} + \varepsilon \quad (3)$$

where $M\left(\delta^i\right)$ is the elevation-dependent mapping function $M(\delta)$ at IPP i, and ε denotes the measurement noise. T_S^i and T_V^i are the STEC and VTEC at IPP i, respectively. b_{RDCB} and b_{SDCB} are the receiver and satellites DCBs, respectively. In practice, the resulting VTEC, after the described corrections and conversion, is subject to a residual error. This residual encompasses the unmodeled errors such as multipath, measurement noise, and inaccuracies in the mapping function, which cause the retrieved VTEC to deviate from the true value. We assume this collective residual as ξ, and the vertical TEC at IPP i is obtained as:

$$T_V^i = \frac{T_S^i - b_{RDCB} - b_{SDCB}}{M\left(\delta^i\right)} + \xi \quad (4)$$

While the components of ξ exhibit different characteristics, their combined effect on the absolute VTEC value is bounded and acceptably small for our purposes (Jakowski & Hoque, 2019). For BDS satellites, the residual error $|\xi| \leq 1$ TECU (1 TECU = 10^{16} electrons/m^2) is typically observed (Li et al., 2014). Crucially, as our analysis focuses on spatiotemporal gradients, the impact of ξ is further mitigated with differential calculations.

Mathematical formulation of the ionospheric gradient estimation framework

Assuming the short-term stability of receiver biases and LOS geometry (Li et al., 2023; Zhong et al., 2016b), the temporal gradient of TEC at IPP i can be defined as:

$$\frac{\partial T_V^i}{\partial t} = \frac{1}{M\left(\delta^i\right)} \bullet \frac{\Delta T_S^i}{\Delta t} = \frac{1}{M\left(\delta^i\right)} \bullet I_{ROT}^i \quad (5)$$

where I_{ROT}^i is the rate of change of STEC at IPP i, defined as (Pi et al., 1997):

$$I_{\mathrm{ROT}}^{i} = \frac{\Delta T_{\mathrm{S}}^{i}}{\Delta t} = \frac{T_{\mathrm{S}}^{i}(t_2) - T_{\mathrm{S}}^{i}(t_1)}{t_2 - t_1} \tag{6}$$

where t denotes the epoch, and the Δt in this study is 30 s.

The rate of TEC fluctuation, characterized by the Rate Of TEC Index (ROTI), is used to identify ionospheric irregularities. The ROTI is calculated based on the standard deviation of the ROT over a 5 min time interval, defined as (Pi et al., 1997):

$$I_{\mathrm{ROTI}}^{i} = \sqrt{\langle \left(I_{\mathrm{ROT}}^{i}\right)^2 \rangle - \langle I_{\mathrm{ROT}}^{i} \rangle^2} \tag{7}$$

where I_{ROTI}^{i} represents ROTI at IPP i. $\langle \bullet \rangle$ denotes the mean averaging operator over a 5 min period.

Figure 2 shows the basic relationship between two GEO IPPs. The spatial gradient, is estimated as the TEC difference along the inter-IPP vector of two IPPs (i and j) at the same epoch, defined as (Jakowski & Hoque, 2019):

$$\left.\frac{\partial T_{\mathrm{V}}^{(i,j)}}{\partial S^{(i,j)}}\right|_t = \left(\frac{T_{\mathrm{S}}^{i}}{M\left(\delta^{i}\right)} - \frac{T_{\mathrm{S}}^{j}}{M\left(\delta^{j}\right)}\right) \bullet \frac{1}{S^{(i,j)}} + \frac{1}{S^{(i,j)}} \bullet \Delta\xi \tag{8}$$

where $S^{(i,j)}$ is the great-circle distance between i and j on the ionospheric thin shell at altitude of 400 km. The influence of the residual error $\Delta\xi$ on the gradient estimation is reduced by a scaling factor inversely proportional to $S^{(i,j)}$. The direction of the inter-IPP vector is defined by the azimuth angle $\theta^{(i,j)}$. The magnitude of the spatial TEC gradient along this vector is defined as:

$$\nabla T_{\mathrm{V}}^{(i,j)}(t) = \left|\left.\frac{\partial T_{\mathrm{V}}^{(i,j)}}{\partial S^{(i,j)}}\right|_t\right| \tag{9}$$

where $|\bullet|$ denotes the absolute value. Based on the azimuth angle $\theta^{(i,j)}$, the zonal (x) and meridional (y) components of the spatial gradient are estimated as:

$$\left.\frac{\partial T_{\mathrm{V}}^{(i,j)}}{\partial x}\right|_t = \nabla T_{\mathrm{V}}^{(i,j)}(t) \bullet \sin\theta^{(i,j)} \tag{10}$$

$$\left.\frac{\partial T_{\mathrm{V}}^{(i,j)}}{\partial y}\right|_t = \nabla T_{\mathrm{V}}^{(i,j)}(t) \bullet \cos\theta^{(i,j)} \tag{11}$$

As GEO satellites are stationary, the spatial gradients at the same location at the next epoch can be defined as:

$$\left.\frac{\partial T_{\mathrm{V}}^{(i,j)}}{\partial x}\right|_{t+\Delta t} = \nabla T_{\mathrm{V}}^{(i,j)}(t+\Delta t) \bullet \sin\theta^{(i,j)} \tag{12}$$

$$\left.\frac{\partial T_{\mathrm{V}}^{(i,j)}}{\partial y}\right|_{t+\Delta t} = \nabla T_{\mathrm{V}}^{(i,j)}(t+\Delta t) \bullet \cos\theta^{(i,j)} \tag{13}$$

Under the assumption of a fixed GEO geometry and small Δt, the temporal variation of the spatial gradient can be related to the spatial variation of the temporal gradient:

$$\frac{\partial^2 T_{\mathrm{V}}^{(i,j)}}{\partial x\,\partial t} \approx \left(\left|\frac{\partial T_{\mathrm{V}}^{i}}{\partial t} - \frac{\partial T_{\mathrm{V}}^{j}}{\partial t}\right| \bullet \frac{\sin\theta^{(i,j)}}{S^{(i,j)}}\right) = \frac{\partial^2 T_{\mathrm{V}}^{(i,j)}}{\partial t\,\partial x} \tag{14}$$

$$\frac{\partial^2 T_{\mathrm{V}}^{(i,j)}}{\partial y\,\partial t} \approx \left(\left|\frac{\partial T_{\mathrm{V}}^{i}}{\partial t} - \frac{\partial T_{\mathrm{V}}^{j}}{\partial t}\right| \bullet \frac{\cos\theta^{(i,j)}}{S^{(i,j)}}\right) = \frac{\partial^2 T_{\mathrm{V}}^{(i,j)}}{\partial t\,\partial y} \tag{15}$$

The approximate mathematical equivalence between the temporal variation of the ionospheric TEC spatial gradient and the spatial variation of the temporal gradient ($\frac{\partial^2 T_{\mathrm{V}}}{\partial t\,\partial S} \approx \frac{\partial^2 T_{\mathrm{V}}}{\partial S\,\partial t}$) serves as a rigorous internal consistency check of the GEO-based monitoring framework. The stationary geometry of GEO satellites eliminates motion-induced artifacts, enabling high-precision estimation of spatial and temporal gradients without the need for motion correction. This geometric invariance enhances the fidelity of gradient estimation and highlights the framework's ability to isolate true ionospheric

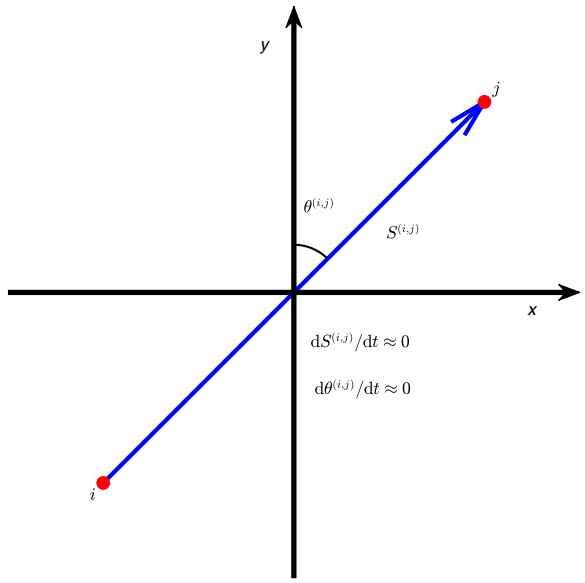

Fig. 2 The inter-IPP vector connects two IPPs, i and j. Its magnitude $S^{(i,j)}$ is the great-circle distance on the ionospheric thin shell (altitude 400 km), and $\theta^{(i,j)}$ denotes the azimuth of the vector measured clockwise from north within the range of $[0, 2\pi)$. As both $dS^{(i,j)}/dt \approx 0$ and $d\theta^{(i,j)}/dt \approx 0$, the vector geometry remains invariant

variability from observational noise. Mathematically, the equality of mixed second-order partial derivatives holds only if the TEC field is continuously differentiable in both space and time. Thus, the deviations from this equality, which are expressed as non-commutativity ($\frac{\partial^2 T_V}{\partial t\,\partial S} \neq \frac{\partial^2 T_V}{\partial S\,\partial t}$), serve as indicators of nonlinear or discontinuous ionospheric processes. For instance, the generation and drift of EPBs introduce coupled space–time disturbances that disrupt a smooth TEC evolution, manifesting as measurable asymmetry in mixed derivatives (Li et al., 2021a, 2021b). These theoretical predictions can be empirically verified using GNSS observations.

Figure 3 shows the spatial gradient of TEC (∇T_V), VTEC, mixed partial derivative asymmetry ($\frac{\partial^2 T_V}{\partial t\,\partial S} - \frac{\partial^2 T_V}{\partial S\,\partial t}$), and ROTI at a single station (20 °N, 110 °E) and in a regional domain (20 °N–30 °N, 110 °E–120 °E) on 2024-09-21 (quiet day). Notably, the fluctuations in ROTI (Fig. 3e) are closely associated with EPB activity (Zhang et al., 2025). The short gaps in the gradient time series occur when no inter-IPP vector midpoint falls within a specific $0.25° \times 0.25°$ grid cell at a given epoch. At the single station, the mixed partial derivatives remain nearly equivalent under conditions but diverge significantly during EPB occurrences (Fig. 3c), which indicates enhanced nonlinearity and plasma instability. In the regional domain, the increases in spatial gradients coincide with TEC enhancements (Fig. 3b), while asymmetry in the mixed partial derivatives peaks during EIA development and EPB events (Fig. 3d, f). These results suggest that disturbed conditions induce nonlinear dynamics that violate the assumption

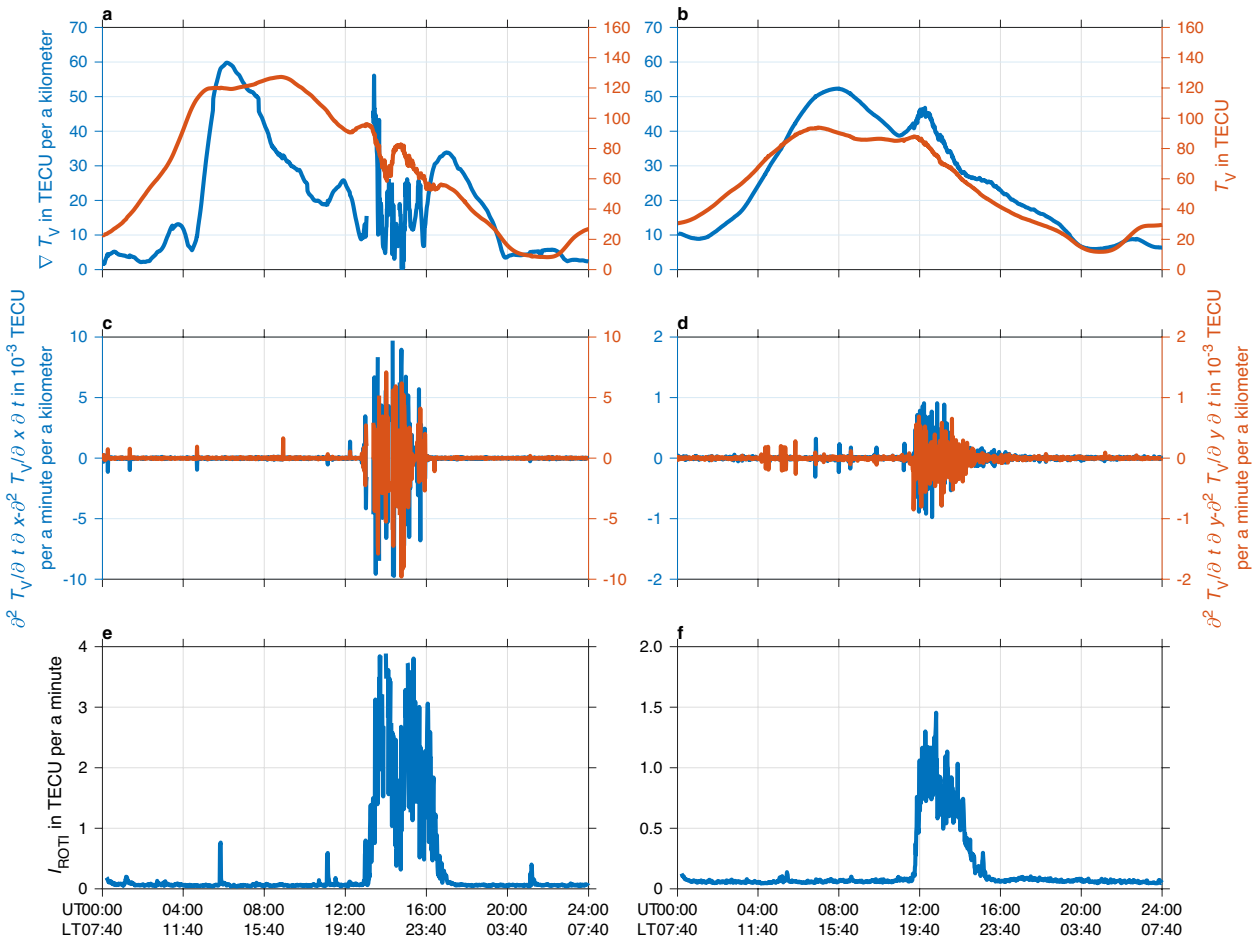

Fig. 3 Variations of ionospheric parameters as a function of Universe Time (UT)/Local Time (LT) (115 °E) on 2024–09-21. The left panels (**a**, **c**, and **e**) refer to a single station (20 °N, 110 °E), while the right panels (**b**, **d**, and **f**) show averages over the regional domain (20 °N–30 °N, 110 °E–120 °E). Note that all data are estimated using five GEO satellites. Panels **a** and **b** show spatial gradient (blue line), and VTEC (orange line). Panels **c** and **d** show mixed partial derivative asymmetry along the east–west direction (blue line), and north–south direction (orange line). Panels **e** and **f** show ROTI values

of linear spatiotemporal evolution. Overall, the observed consistency of mixed derivatives in quiet conditions and their measurable divergence during EPBs confirm the robustness of the GEO-based framework, establishing it as a reliable diagnostic tool for both linear and nonlinear ionospheric processes. Additionally, this detection of nonlinear processes requires only carrier phase measurements at two adjacent epochs, without a need for DCB calibration or long time-series data.

Since the spatial-gradient field is represented as $0.25^\circ \times 0.25^\circ$ grid-cell means, we assess whether ionospheric TEC variability is resolved at this scale using the within-cell standard deviation of the contributing ∇T_V samples. It is defined as:

$$\sigma(\nabla T_V) = \sqrt{\langle (\nabla T_V)^2 \rangle - \langle \nabla T_V \rangle^2} \tag{16}$$

where $\langle \bullet \rangle$ denotes the arithmetic mean of all samples within the grid cell.

Case study I: diurnal evolution of the EIA

The EIA is one of the most prominent and regularly occurring ionospheric structures in low latitudes (Balan et al., 2018). As elucidated by the equatorial plasma fountain theory, plasmas drift upward and disperse along geomagnetic field lines, generating an electron-density trough over the magnetic equator and forming crests at approximately 15 °N–20 °N and 15 °S–20 °S magnetic latitude (Chen et al., 2023; Nigussie et al., 2022). This section investigates the EIA's diurnal development in both large-scale and regional domains, using the GEO-based monitoring framework to characterize its formation mechanisms and spatiotemporal structure.

Figure 4 shows the TEC and its derived spatiotemporal gradients over a broad region (15 °N–50 °N, 95 °E–135 °E) at 13:40 LT on 2024-09-21. In Fig. 4b, two pronounced

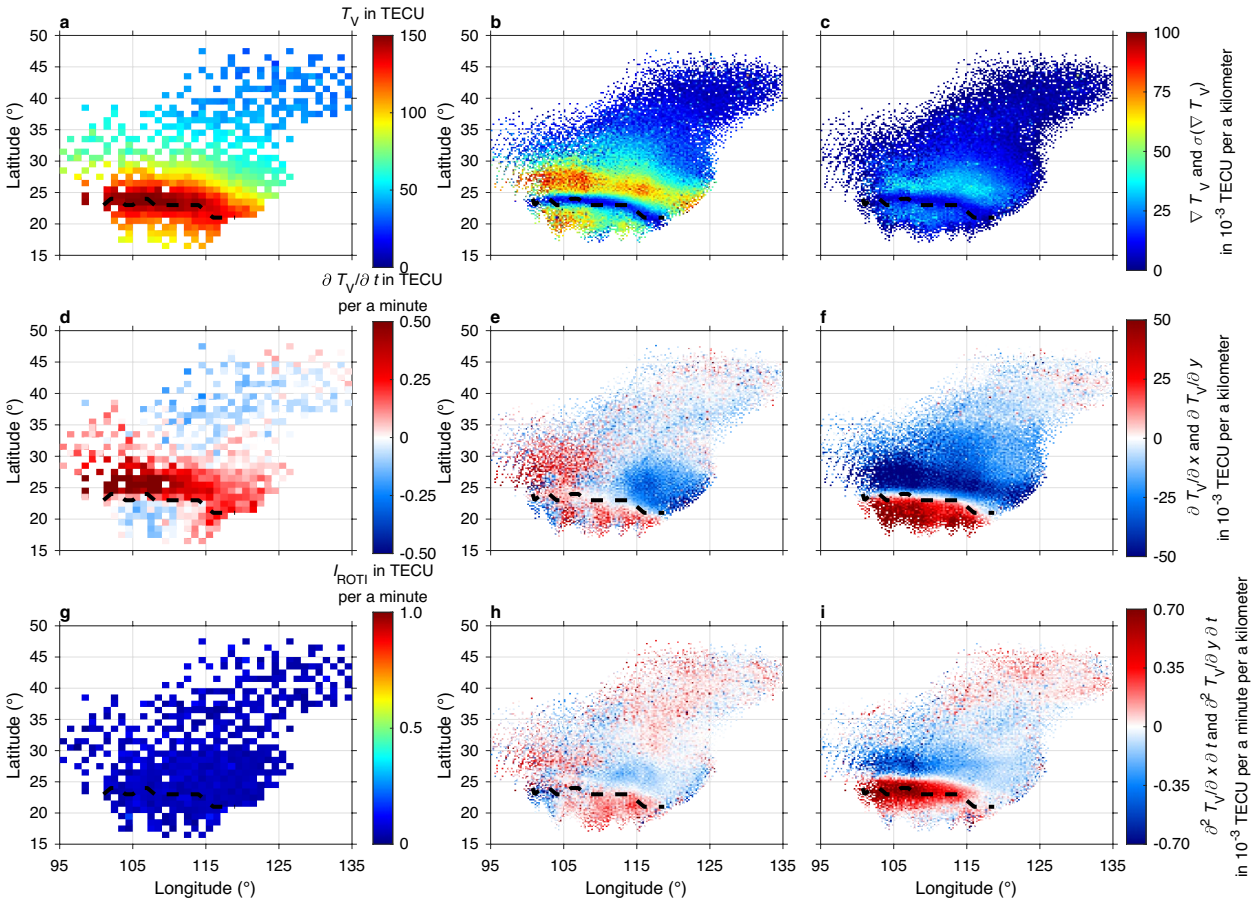

Fig. 4 Variations of ionospheric parameters over the region (15 °N–50 °N, 95°E-135°E) as a function of geographic longitude and latitude at 13:40 LT (115 °E) on 2024-09-21. All panels display grid-mean values. Panels **b**, **c**, **e**, **f**, **h** and **i** use a $0.25^\circ \times 0.25^\circ$ grid, while panels **a**, **d** and **g** use a $1^\circ \times 1^\circ$ grid. The **a** VTEC, **b** spatial gradient, **c** within-cell standard deviation, **d** temporal gradient, **e** zonal spatial gradient, **f** meridional spatial gradient, **g** ROTI, **h** zonal spatial gradient component of temporal gradient, and **i** meridional spatial gradient component of temporal gradient are shown in panels. The black dashed line indicates the VTEC peak region calculated from panel **a**. The positive directions of the spatial gradient are northward and eastward

spatial gradient bands flank 25 °N, which corresponds to the weakening TEC peak of the EIA toward both northern and southern latitudes in Fig. 4a. These features are corroborated by zonal and meridional gradients in Fig. 4e, f, respectively. The north–south (y-direction) TEC gradients (Fig. 4f) illustrate diffusion from the crest region toward higher and lower latitudes, while east–west (x-direction) gradients (Fig. 4e) highlight longitudinal asymmetry in plasma distribution. Figure 4c shows enhanced $\sigma(\nabla T_V)$ values along the EIA flanks, suggesting unresolved sub grid-scale structures. Figure 4d shows rapid TEC enhancement near the EIA crest, indicative of linear plasma transport and in situ generation processes. Figure 4h, i show the zonal and meridional components of the mixed spatiotemporal gradient ($\frac{\partial^2 T_V}{\partial S\, \partial t}$), which approximate the local advective effects of TEC variation. The agreement between spatial patterns in Fig. 4h, i and their spatial-only counterparts (Fig. 4e, f) suggests that the early-stage EIA evolution is dominated by transport-driven dynamics.

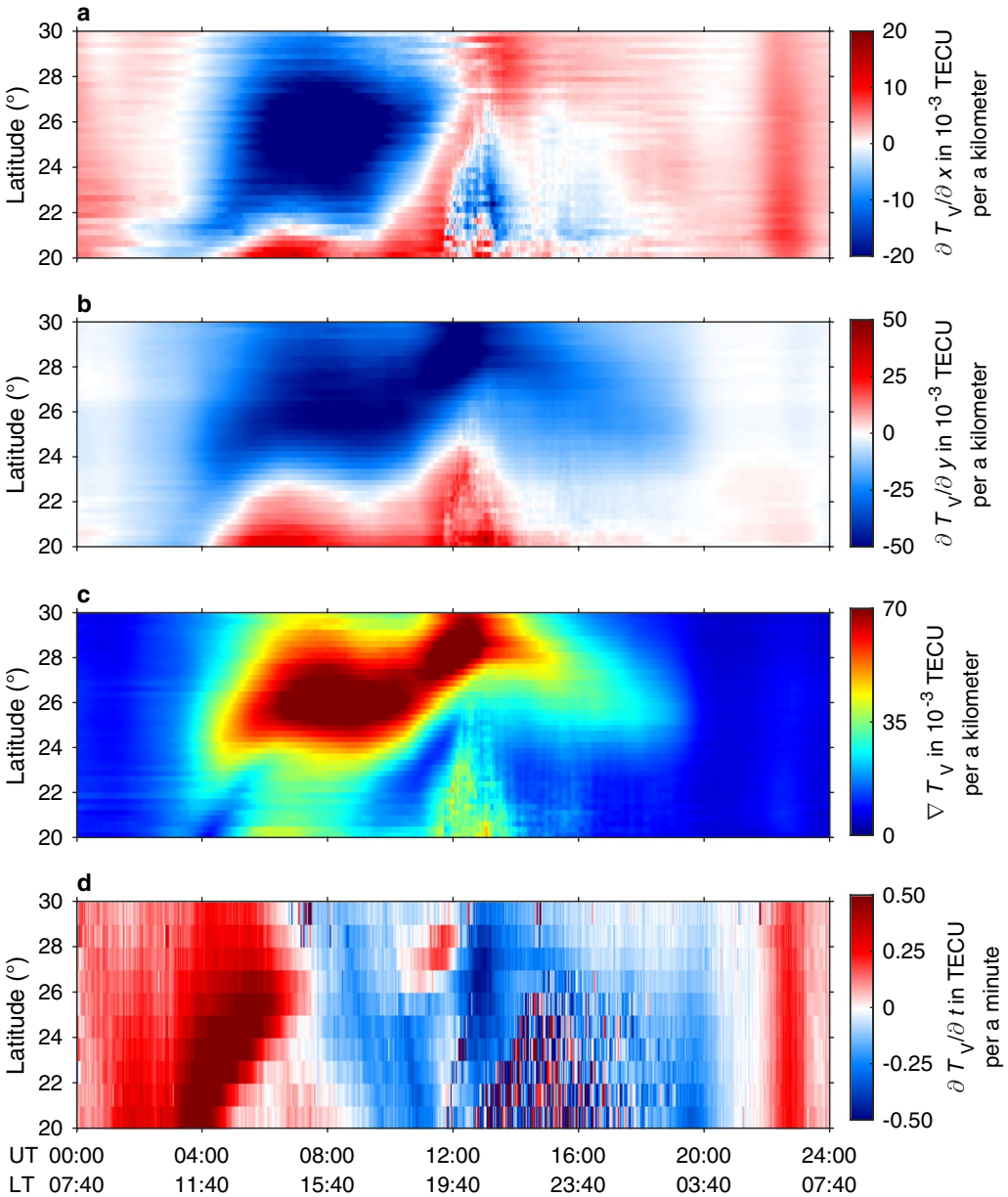

Fig. 5 Variations of the zonal mean of the **a** zonal spatial gradient, **b** meridional spatial gradient, **c** spatial gradient, and **d** temporal gradient over a regional domain (20 °N–30 °N, 110 °E–120 °E) as a function of UT/LT (115 °E) on 2024-09-21

Figure 5 shows the zonal (east–west) means of selected parameters in a regional domain (20 °N–30 °N, 110 °E–120 °E), capturing localized EIA evolution. From 03:40 to 11:40 LT, Fig. 5a shows a positive eastward TEC gradient emerges as the solar terminator migrates eastward, with sunlit regions experiencing stronger ionization. From 11:40 LT to 19:40 LT, corresponding to the EIA's formation, peak, and weakening phases, with meridional TEC troughs forming and intensifying. After 19:40 LT, EPB-induced plasma density depletions erode the southern gradient structure. Figure 5b displays meridional TEC variation, showing an increase followed by a decrease, marking the crest region. Figure 5c reveals persistent EIA-driven spatial gradient structures flanking the TEC peak from 11:40 LT to 17:40 LT, with the southern gradient weakening after 17:40 LT, while the northern gradient persists until 01:40 LT. Figure 5d highlights the dominance of linear processes (TEC transport or local generation) during early EIA formation (11:40–14:40 LT). Figure 5d confirms that early-stage EIA growth (11:40–14:40 LT) is dominated by linear processes, followed by enhanced TEC and EPB-linked fluctuations from 19:40–01:40 LT that disrupt the southern EIA structure.

Figure 6 complements the analysis with meridional (north–south) means over the same region. Figure 6a reveals the zonal gradient structures driven by EPB drift, where plasma density depletions (TEC troughs) generate opposing positive/negative gradients along their eastern and western boundaries, respectively. This result explains the stronger zonal erosion of gradient structures in Fig. 5. Figure 5b shows longitudinal TEC variations within the EIA, highlighting east–west asymmetry in ionization density distribution. EPBs are evident from 19:40 to 23:40 LT in Fig. 5c, d, exhibiting eastward drift prior to dissipation.

Case study II: life-cycle of EPBs

EPBs characterized by density-depleted regions in the ionosphere, are a major concern in space weather studies due to their disruptive effects on satellite-based communication and navigation systems (Tang et al., 2024). This section examines the dynamic behavior of EPBs using spatiotemporal gradient diagnostics enabled by the GEO-based monitoring framework.

Figure 7 shows the ionospheric response at 22:40 LT on 2024-09-21 during the eastward drift of an active EPB. Figure 7a shows a distinct TEC depletion spanning 105 °E–115 °E in longitude, which is confirmed by the ROTI-based EPB detection in Fig. 7g. This EPB extends northward to 25 °N, with a westward-tilted morphology. Figure 7b shows sharp spatial TEC gradients flanking near 110 °E around 20 °N–25 °N. This panel also shows a zonal enhancement belt of ∇T_V near 25 °N, which indicates a rapid northward decrease in VTEC. This feature marks the northern boundary of the TEC variations. Figure 7c highlights that the internal spatial scale of EPB-induced gradients is notably finer than the large-scale background gradients around 25 °N, reflecting localized plasma irregularities. Figure 7d demonstrates that plasma density inhomogeneity within the EPB drives rapid temporal gradient fluctuations. The zonal gradient field (Fig. 7e) displays opposing positive and negative extrema on either side of the EPB trough, while Fig. 7f reveals weaker but discernible meridional asymmetry, with the EPB slightly intruding into the background northern EIA gradient. Figure 7g, h further exhibit elevated mixed partial derivative asymmetries, which indicates the presence of strong nonlinear dynamics coincident with the EPB structure (Fig. 3d), thereby validating the sensitivity of the framework to space–time coupled plasma processes.

Figure 8 tracks the evolution of zonal spatial gradients during the EPB's emergence, maturation, and dissipation. The EPB first appears at 20:00 LT near 110 °E and drifts eastward to 115 °E by 23:40 LT. The EPB maintains a consistent morphology of steep gradients flanking its TEC depletion, while the gradient intensity peaks near 22:40 LT and diminishes by 23:40 LT. Interestingly, the EPB's westward tilt angle decreases (clockwise rotation) during growth (20:20–22:40 LT) and increases (counterclockwise rotation) during dissipation (22:40–23:40 LT), suggesting dynamic changes in background electrodynamics and instability development.

Case study III: propagation of LSTIDs

LSTIDs are wave-like perturbations in ionospheric electron density with ranging from hundreds to thousands of kilometers in wavelength, generated by atmospheric gravity waves or magnetospheric activities (Hocke & Schlegel, 1996; Nykiel et al., 2024). These disturbances impact satellite-based communication and positioning by inducing TEC fluctuations that degrade navigation accuracy (Carter et al., 2023). This section analyzes an LSTID event in the Asian sector on 2024-10-11 (Dst = − 308 nT) to demonstrate the framework can resolve large-scale disturbances during geomagnetic storms.

Figure 9 shows the zonal mean of spatiotemporal gradients during an LSTID event of a geomagnetic storm on 2024-10-11. Figure 9d, alternating positive and negative bands in the temporal gradient reflect the southward propagation of LSTID wavefronts, which dissipate around 30 °N–35 °N. Additionally, the northward-propagating structure (in red) between 20 °N and 30 °N represents the daytime low-latitude EIA developing toward higher latitudes. It converges with the

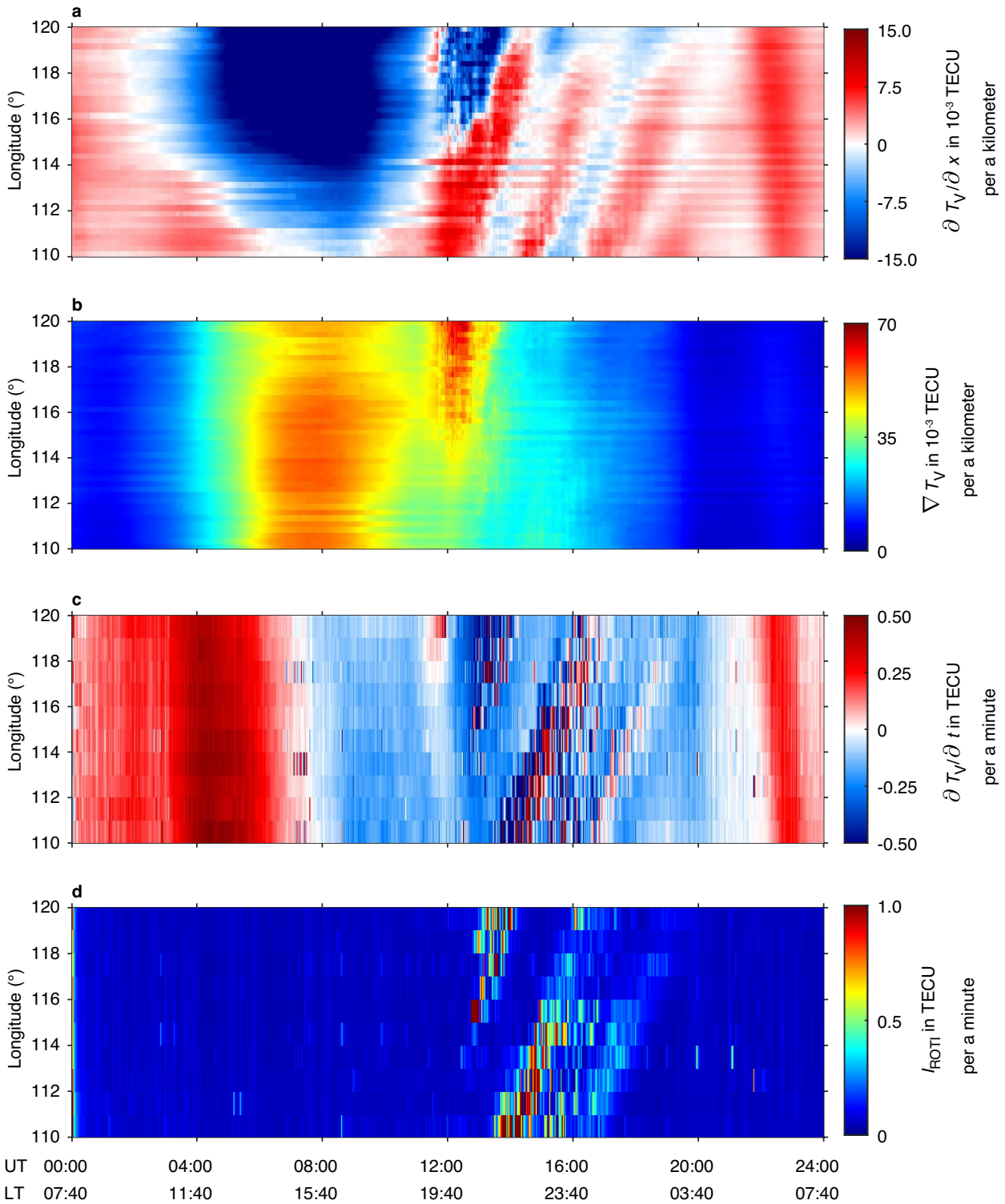

Fig. 6 Variations of the meridional mean of the **a** zonal spatial gradient, **b** spatial gradient, **c** temporal gradient, and **d** ROTI over a regional domain (20°N–30°N, 110°E–120°E) as a function of UT/LT (115 °E) on 2024-09-21

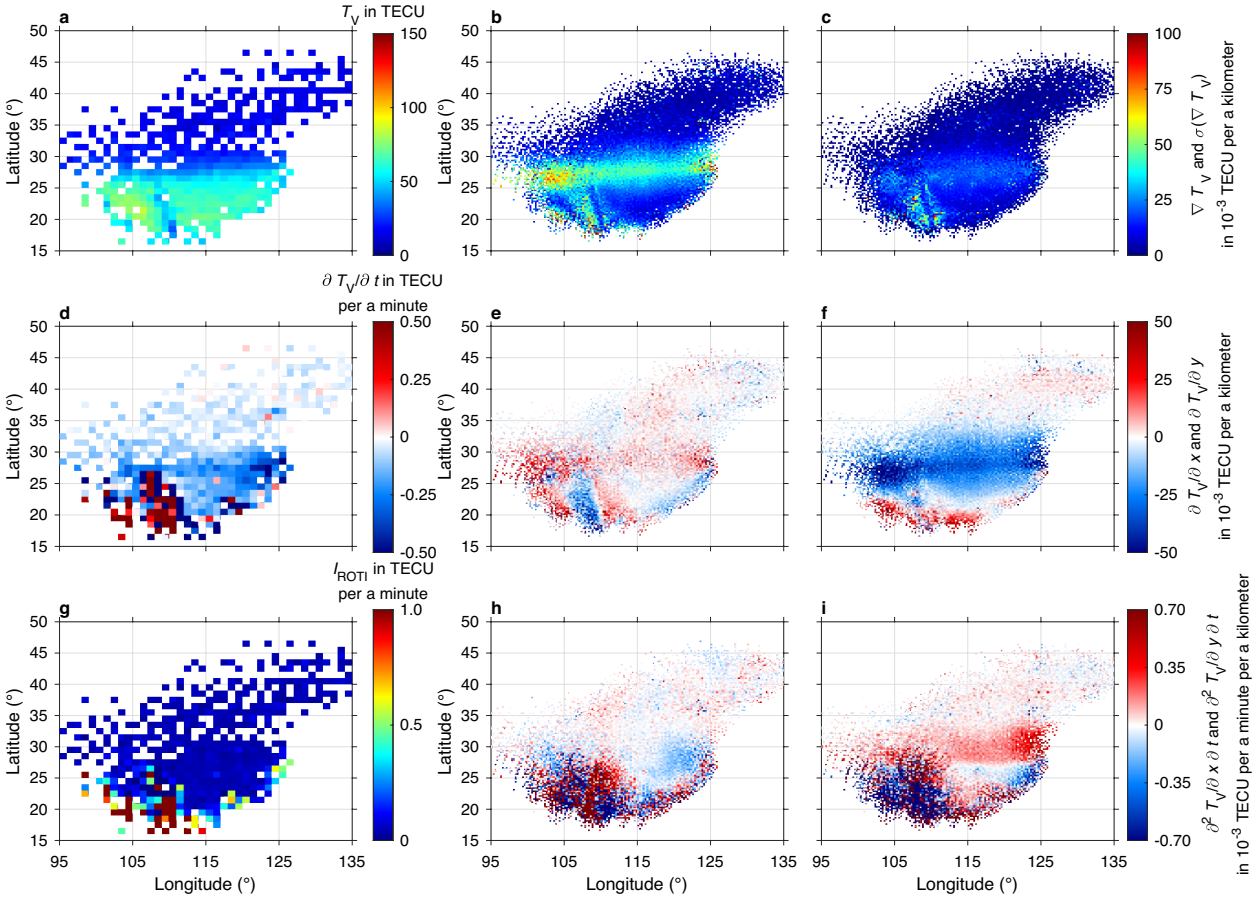

Fig. 7 Variations of ionospheric parameters over the region (15 °N–50 °N, 95 °E–135 °E) as a function of geographic longitude and latitude at 22:40 LT (115 °E) on 2024-09-21. All panels display grid-mean values. Panels **b**, **c**, **e**, **f**, **h** and **i** use a 0.25°×0.25° grid, while panels **a**, **d** and **g** use a 1°×1° grid. The **a** VTEC, **b** spatial gradient, **c** within-cell standard deviation, **d** temporal gradient, **e** zonal spatial gradient, **f** meridional spatial gradient, **g** ROTI, **h** zonal spatial gradient component of temporal gradient, and **i** meridional spatial gradient component of temporal gradient are shown in panels. The positive directions of the spatial gradient are northward and eastward

LSTID around 32 °N near 12:40 LT. The wave exhibits a meridional wavelength of approximately 500 km and a phase speed exceeding 450 m/s near 11:40 LT. Figure 9c shows total spatial gradient signatures that align closely with the temporal variations in Fig. 9d, which indicates the coherence of the disturbance in space and time. Given that LSTIDs predominantly propagate meridionally, their influence is most prominent in the north–south gradient component (Fig. 9b), with minimal expression in the zonal direction (Fig. 9a).

Figure 10 provides a snapshot of LSTID-induced ionospheric variations at 10:30 LT. In Fig. 10b, three prominent spatial gradient structures are observed at 25 °N, 30 °N, and 40 °N. The 25 °N gradient coincides with a steep TEC decay slope in Fig. 10a and the northern boundary of a rapid TEC enhancement zone in Fig. 10d. This structure aligns with the northward-propagating EIA feature (in red, Fig. 9d). In Fig. 10d, temporal gradients exhibit alternating TID crests and troughs, with a latitudinal trough (~ 5°, 500 km) demarcated near 35 °N. The 30 °N and 40 °N gradients align with TID crests in Fig. 10d, appearing as negative meridional gradients in Fig. 10f (TEC decreasing poleward), a hallmark of LSTID-induced electron density enhancements. Figure 10i resolves TID crest positions via advection terms, highlighting plasma-dominated transition zones at 30 °N and 40 °N. The absence of significant sub-grid variability in Fig. 10c underscores the LSTID's dominance at scales exceeding tens of kilometers.

Figure 11 shows the zonal-mean latitudinal profiles of key spatiotemporal gradients to characterize the phase structure of the TID wave at a fixed epoch. This figure provides a clear view on how the phase structure of the TID wave is represented with different gradient metrics. In Fig. 11a, the $\frac{\partial T_V}{\partial t}$ curve delineates the full spatial distribution of a TID phase at a single epoch. Positive values correspond to local TEC enhancement (i.e., positive phase), while negative values indicate depletion (negative

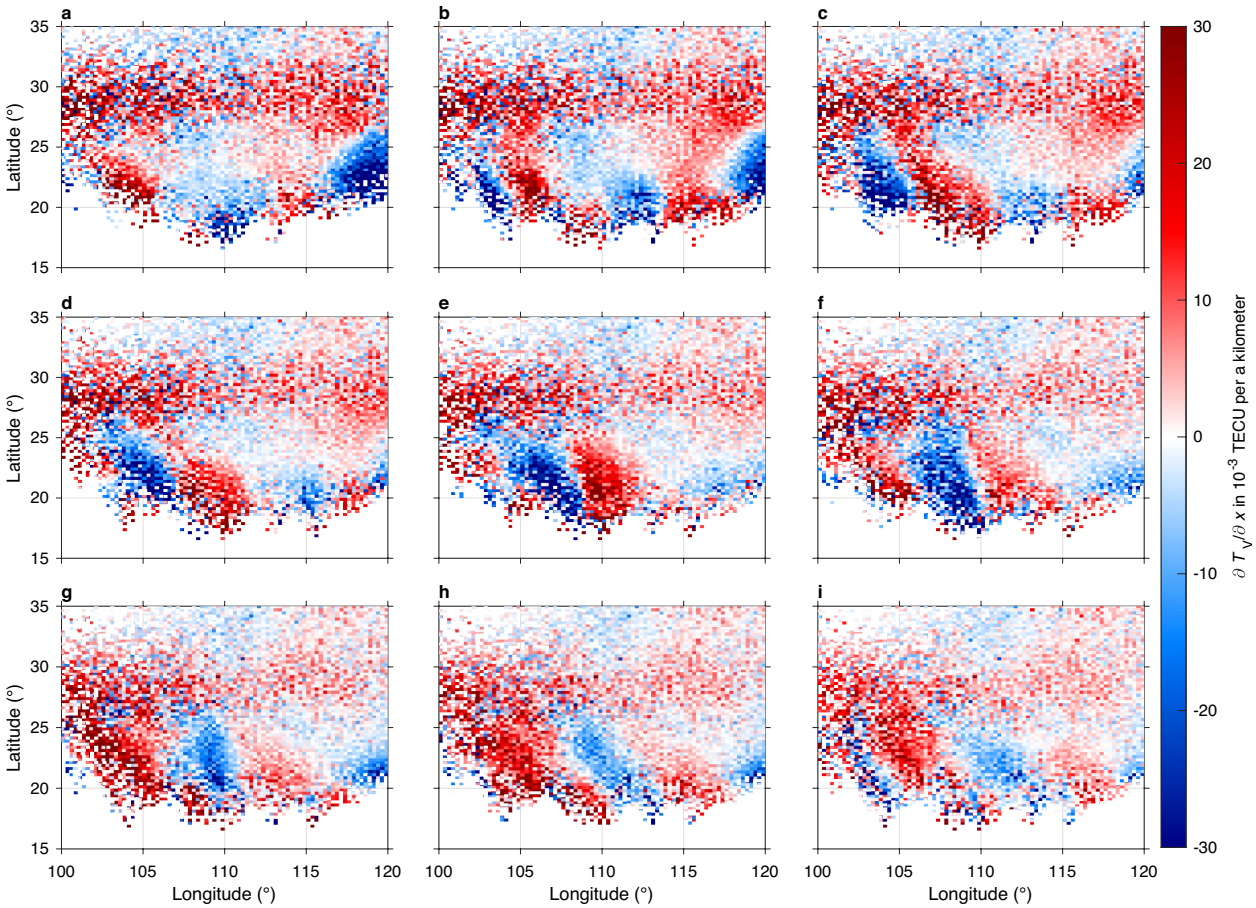

Fig. 8 Variations of the zonal spatial gradient $\frac{\partial T_V}{\partial x}$ over a regional domain (15 °N–35 °N, 100 °E–120 °E) as a function of LT (115°E) on 2024–09-21. The time span ranges from 20:00 LT to 22:40 LT, with panel **a** at 20:00 LT and panel **i** at 22:40 LT. Each panel is presented at 20 min intervals. All panels display grid-mean values with a 0.25°×0.25° grid

phase). The gray shading marks the zero-crossing points of $\frac{\partial T_V}{\partial t}$, which represent the transition zones between positive and negative phases of the wave. These positions closely align with the extrema in Fig. 11c, which indicates that the mixed gradient $\frac{\partial^2 T_V}{\partial y\,\partial t}$ effectively represents the latitudinal variation of the temporal TEC gradient. Physically, $\frac{\partial^2 T_V}{\partial y\,\partial t}$ captures how rapidly the temporal evolution of TEC changes in space, and thus serves as a diagnostic proxy for the spatial inhomogeneity of the wave phase. Figure 11c shows that its zero-crossing points correspond to local peaks or troughs of the $\frac{\partial T_V}{\partial t}$ curve, while its extrema correspond to inflection points or phase transitions within the TID. Figure 11b presents the $\frac{\partial T_V}{\partial y}$, revealing the steady-state spatial slope of the wave. Notably, the steepest gradients appear within the negative phase of the TID, suggesting that TEC gradients are most pronounced where the wave induces depletion. Overall, these three quantities jointly describe the TID's spatiotemporal structure: $\frac{\partial T_V}{\partial t}$ reveals the instantaneous phase state, $\frac{\partial T_V}{\partial y}$ characterizes the spatial slope induced by the wave, and $\frac{\partial^2 T_V}{\partial y\,\partial t}$ captures the spatial variability of temporal evolution.

Discussion

Conventional monitoring of ionosphere relies on platforms such as MEO, GNSS Radio Occultation (GNSS-RO), and LEO satellites, together with Global Ionospheric Maps (GIMs). GNSS-RO and LEO in-situ missions provide observations at different altitudes (Cherniak et al., 2021; Wood et al., 2022). GIMs are reconstructed from worldwide MEO observations using interpolation and modeling, which ensures global coverage (Li et al., 2021a, 2021b). These approaches are effective for climatology, large-scale patterns, and event snapshots. However, they seldom resolve the transient and fine-scale processes that govern ionospheric dynamics (Astafyeva et al., 2015; Chen et al., 2017;

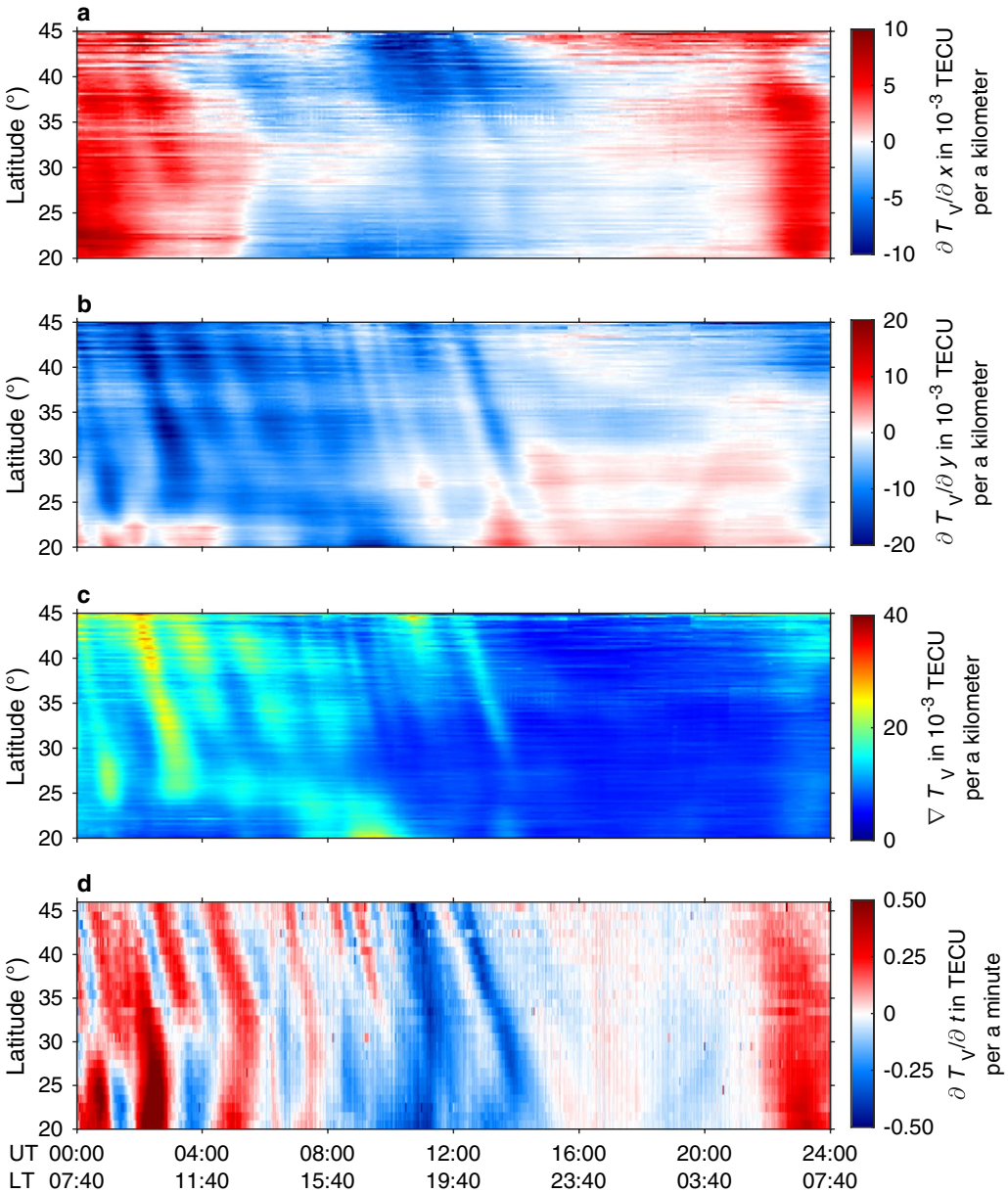

Fig. 9 Variations of the zonal mean of the **a** zonal spatial gradient, **b** meridional spatial gradient, **c** spatial gradient, and **d** temporal gradient over a regional domain (20 °N–45 °N, 95 °E–135 °E) as a function of UT/LT (115 °E) on 2024-10-11

Cherniak et al., 2025; Li et al., 2020). The limitation arises from sparse and asynchronous sampling, moving pierce points, and interpolation smoothing. The vector-based sensing design of the fixed-geometry framework preserves the direction and sign information of the ionospheric dynamics, providing a physically consistent and continuous view of horizontal structure. This capability fills a critical gap in multi-platform ionospheric diagnosis.

Deciphering the dynamics of large-scale ionospheric structures such as the EIA and LSTIDs requires resolving fine spatiotemporal features (Chen et al., 2024; Liu et al., 2023; Sun et al., 2024; Zhong et al., 2019). The gradient vector field derived with the framework avoids interpolation induced information loss, and enables direct observation of the ionospheric dynamics, including the instantaneous EIA crest location and the phase of LSTID fronts. For the EIA, the field resolves steep meridional spatial gradients and sign reversals across

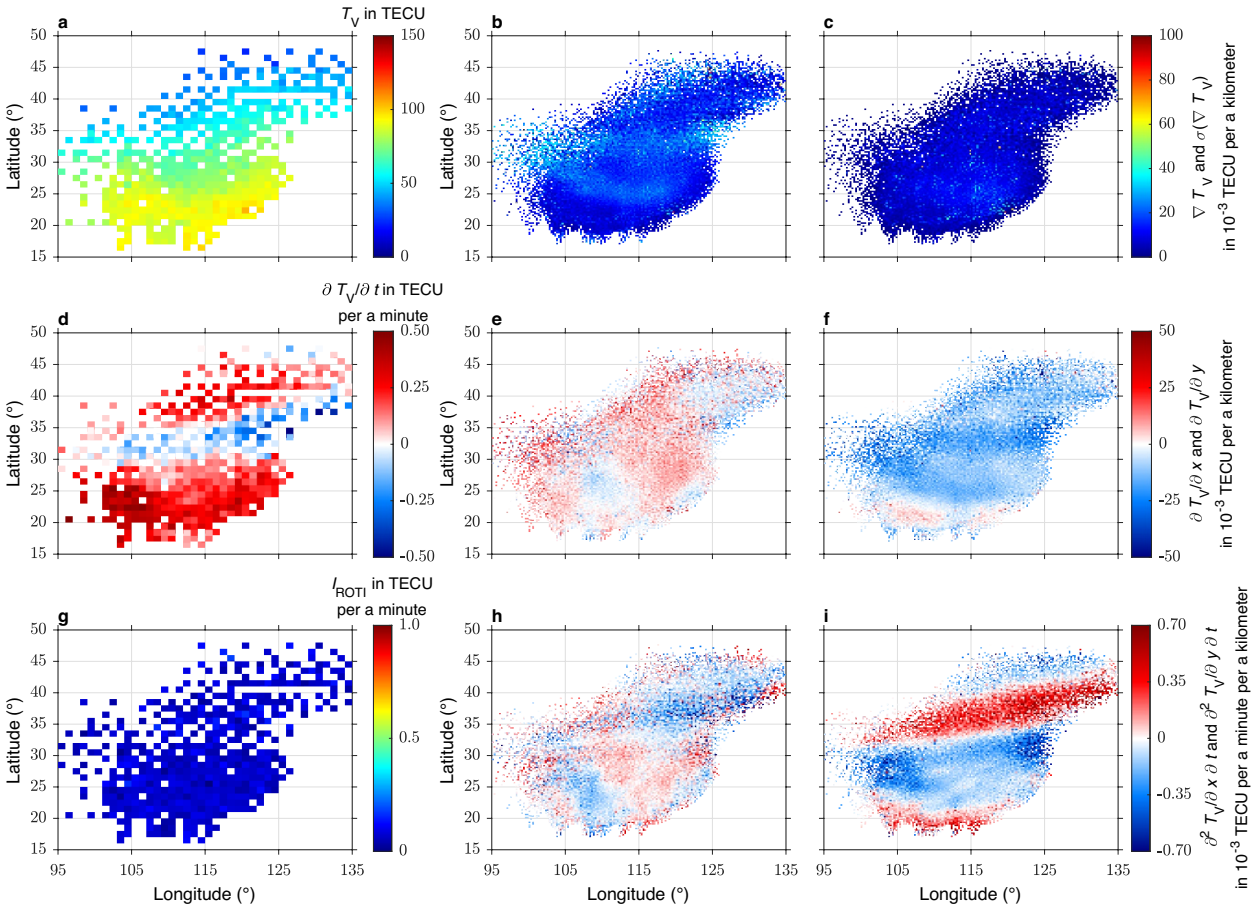

Fig. 10 Variations of ionospheric parameters over the region (15 °N–50 °N, 95 °E–135 °E) as a function of geographic longitude and latitude at 10:30 LT (115°E) on 2024-10-11. All panels display grid-mean values. Panels **b**, **c**, **e**, **f**, **h** and **i** use a 0.25°×0.25° grid, while panels **a**, **d** and **g** use a 1°×1° grid. The **a** VTEC, **b** spatial gradient, **c** within-cell standard deviation, **d** temporal gradient, **e** zonal spatial gradient, **f** meridional spatial gradient, **g** ROTI, **h** zonal spatial gradient component of temporal gradient, and **i** meridional spatial gradient component of temporal gradient are shown in panels. The positive directions of the spatial gradient are northward and eastward

the crest. And the high spatiotemporal continuity of field also allows tracking of crest motion and longitudinal asymmetry evolution. These observations can provide direct evidence for understanding regional variations in the plasma fountain and the influence of background electrodynamics, including neutral winds and electric fields. The simultaneous estimation of multiple TEC based quantities can be used to diagnose the underlying transport and local production of plasma. For LSTIDs, joint analysis of temporal gradients, spatial gradients, and mixed spatiotemporal derivatives identifies the crests, troughs, front boundaries, and spatial inhomogeneity in phase evolution. This multi-parameter view provides the direct evidence of wave–background coupling process and supports detailed characterization of wave energy propagation and dissipation beyond simple front detection. Overall, the framework can move EIA and LSTID studies beyond static summaries and points toward quantitative, real-time diagnosis of internal physical processes.

EPBs are characterized by steep plasma density gradients and associated signal scintillations (Li & Jiang, 2024). Conventional indices, such as ROTI and phase or amplitude scintillation metrics detect activity but lose the sign and direction information of ionospheric dynamics (Affonso et al., 2022; Li et al., 2021a, 2021b; Zhang et al., 2025). This limitation arises from time-series analyses that summarize signal amplitude or variability. In contrast, the gradient sensing allows precise localization of bubble walls and identification of depletion trough at a single epoch. Bubble walls are manifested as meridional belts of large ∇T_V. The depletion trough sits where the zonal gradient $\frac{\partial T_V}{\partial x}$ change sign. The magnitude of $\frac{\partial T_V}{\partial x}$ separates growth from decay along the wall. During EPB events, the commutation residual $\frac{\partial^2 T_V}{\partial t\, \partial S} - \frac{\partial^2 T_V}{\partial S\, \partial t}$ increases

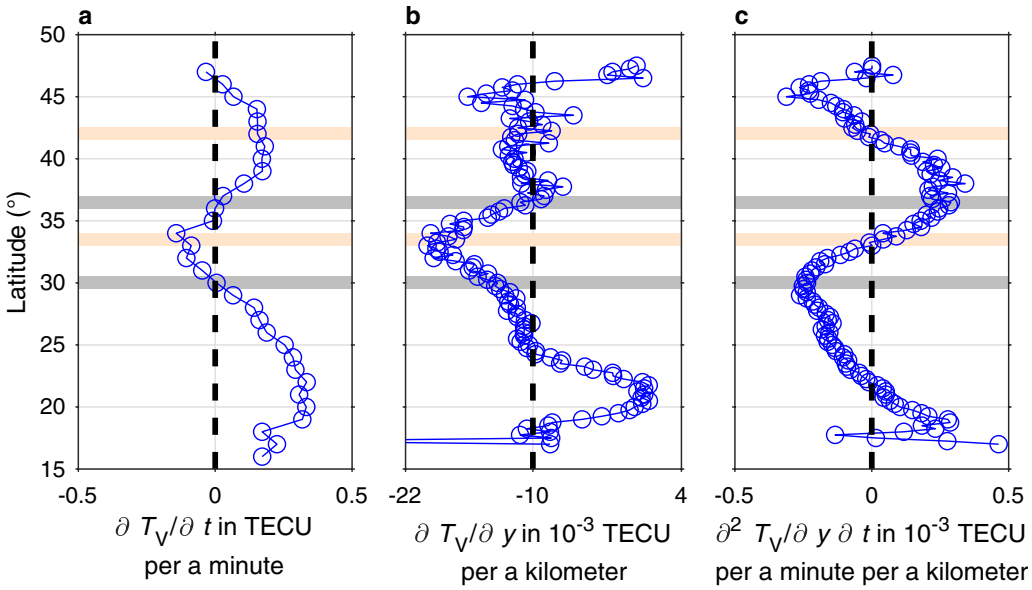

Fig. 11 Zonal mean latitudinal profiles of **a** temporal gradient, **b** meridional spatial gradient, and **c** meridional component of the mixed gradient at 10:30 LT (115 °E) on 2024-10-11, over the regional domain in Fig. 10. Gray shading highlights the zero-crossing points in $\frac{\partial T_V}{\partial t}$ of panel **a**, while orange shading denotes local extrema of the curve in $\frac{\partial T_V}{\partial t}$. The shading width is 1°

markedly, providing an observational proxy for strong nonlinearity and instability. These morphology-aware, event-level constraints enable near-real-time tracking across longitudinal sectors.

The advantages of the fixed-geometry observation network extend well beyond constructing two-dimensional gradient fields, and offer new pathways to overcome key technical challenges in current ionospheric monitoring. The availability of GEO satellites at multiple longitudes provides a basis for evaluating and refining the conventional single-layer mapping function. In low-latitude regions with vertical structures such as the EIA and EPBs, $\sigma(\nabla T_V)$ serves as a consistency metric for resolving fine-scale ionospheric features. By further comparing gradient responses to identical the structures viewed from different longitudes and elevation angles, the elevation-dependent errors introduced by the thin-shell assumption can be quantified and corrected (Chen et al., 2022; Zhong et al., 2016a). This provides an observational basis for assessing and refining mapping-function formulations, including regionally adaptive effective-height. Additionally, the framework will give new possibilities for monitoring three-dimensional ionospheric structure (Bolmgren et al., 2020; Zhai et al., 2025).

Conclusion

This study presents a novel ionospheric monitoring framework based on a fixed-geometry observation network formed by the stable LOS configuration between GEO satellites and ground-based GNSS receivers. By leveraging the geometric invariance of stationary IPPs and inter-IPP vectors, the framework transforms conventional pointwise TEC sampling into a structure-aware sensing architecture that enables real-time and high-resolution monitoring of ionospheric dynamics across multiple spatial and temporal scales.

A key advantage of the framework lies in its ability to directly extract spatial and temporal TEC gradients with strict geometric consistency, without relying on interpolation or satellite-motion corrections. These gradients provide instantaneous estimates of plasma redistribution, allowing fine-scale disturbances to be distinguished from the slowly varying ionospheric background. The retrieval of mixed partial derivatives further enables the diagnosis of nonlinear processes and plasma instabilities in disturbed conditions. With three representative case studies, we demonstrate the framework can resolve diurnal evolution of equatorial ionization anomalies, track the lifecycle of equatorial plasma bubbles, and characterize the propagation of large-scale traveling ionospheric disturbances. These results illustrate the framework's unique capacity to support dynamic event-scale diagnostics, offering spatial resolution finer than 0.25° and temporal resolution of 30 s over continental scales.

The proposed framework provides a scalable and cost-effective foundation for continental-scale ionospheric monitoring. It bridges the gap between sparse satellite observations and localized ground-based diagnostics, and lays the groundwork for constructing a high-resolution and long-duration ionospheric dataset in the Asian sector. As GNSS infrastructure continues to expand, this approach offers broad applicability for real-time monitoring, modeling, and early warning of ionospheric space weather phenomena.

Acknowledgements
We are grateful to the Chinese Academy of Sciences (CAS, https://data.bdsmart.cn/pub/) and the International GNSS Service (IGS) for providing GNSS data.

Author contributions
NW, and JZ contributed to the conceptualization; ZL, JZ, NW, YH, XW, AL, and RL were involved in the methodology; ZL, and NW assisted in the formal analysis and investigation; ZL and JZ contributed to writing—original draft preparation; ZL, JZ, NW, YH, XW, NJ, MH, and GN helped in writing—review and editing; JZ, NW, YH, and XW acquired the funding; NW, JZ, ZsL, YH, and XW contributed to the resources; JZ, NW, YH, AL, XW, and ZsL contributed to the supervision. All authors have read and agreed to the published version of the manuscript.

Funding
This work was supported by the National Natural Science Foundation of China (42374181, 42374186, 42441814), Key Innovation Team of China Meteorological Administration 'Space Weather Monitoring and Alerting' (CMA2024ZD01), 'Ionospheric Forecast and Alerting' Youth Innovation Team (CMA2024QN09), Shandong Key R&D Program (2024CXGC00116) and Jinan Haiyou Leading Talents Of Industry.

Data availability
The broadcast ephemeris, along with the precise satellite ephemeris and clock products, is accessible at http://www.igs.gnsswhu.cn/index.php. The data underlying this manuscript are available at https://data.bdsmart.cn/pub/campaign/iono/gixgeo. The DCB products are available at https://data.bdsmart.cn/pub/product/bias/.

Declarations

Competing interests
The authors declare no competing interests.

Received: 24 July 2025 Revised: 19 November 2025 Accepted: 21 November 2025
Published online: 08 December 2025

References

Affonso, B. J., Moraes, A., Sousasantos, J., Marini-Pereira, L., & Pullen, S. (2022). Strong ionospheric spatial gradient events induced by signal propagation paths aligned with equatorial plasma bubbles. *IEEE Transactions on Aerospace and Electronic Systems, 58*(4), 2868–2879. https://doi.org/10.1109/TAES.2022.3144622

Astafyeva, E., Zakharenkova, I., & Förster, M. (2015). Ionospheric response to the 2015 St. Patrick's day storm: A global multi-instrumental overview. *Journal of Geophysical Research: Space Physics, 120*(10), 9023–9037. https://doi.org/10.1002/2015JA021629

Balan, N., Liu, L., Le, H., Institute of Geology and Geophysics, Chinese Academy of Sciences, Beijing 100029, China. (2018). A brief review of equatorial ionization anomaly and ionospheric irregularities. *Earth and Planetary Physics, 2*(4), 1–19. https://doi.org/10.26464/epp2018025

Bolmgren, K., Mitchell, C., Bruno, J., & Bust, G. (2020). Tomographic imaging of traveling ionospheric disturbances using GNSS and geostationary satellite observations. *Journal of Geophysical Research: Space Physics, 125*(3), Article e2019JA027551. https://doi.org/10.1029/2019JA027551

Buonsanto, M. J. (1999). Ionospheric storms—a review. *Space Science Reviews, 88*(3), 563–601. https://doi.org/10.1023/A:1005107532631

Carter, B. A., Pradipta, R., Dao, T., Currie, J. L., Choy, S., Wilkinson, P., Maher, P., Marshall, R., Harima, K., Le Huy, M., Nguyen Chien, T., Nguyen Ha, T., & Harris, T. J. (2023). The ionospheric effects of the 2022 Hunga Tonga volcano eruption and the associated impacts on GPS precise point positioning across the Australian region. *Space Weather, 21*(5), Article e2023SW003476. https://doi.org/10.1029/2023SW003476

Chen, J., Zhong, J., Cai, X., Hao, Y., Cai, L., Wan, X., Li, Q., Tang, Z., Song, X., Han, H., Kuai, J., & Cai, L. (2024). Characteristics of longitudinal discontinuity over nighttime equatorial ionization anomaly crests with multiple observations. *Journal of Geophysical Research: Space Physics, 129*(11), Article e2024JA033133. https://doi.org/10.1029/2024JA033133

Chen, J., Zhong, J., Hao, Y., Wan, X., Li, Q., Tang, Z., Song, X., Han, H., Wang, K., Kuai, J., & Ren, A. (2023). Horizontal spatial correlation of the ionospheric day-to-day variations at low latitudes based on GOLD Nmax data. *Space Weather, 21*(12), Article e2023SW003627. https://doi.org/10.1029/2023SW003627

Chen, P., Wang, R., Yao, Y., An, Z., & Wang, Z. (2022). A novel ionospheric mapping function modeling at regional scale using empirical orthogonal functions and GNSS data. *Journal of Geodesy, 96*(5), 34. https://doi.org/10.1007/s00190-022-01624-x

Chen, P., Yao, Y., & Yao, W. (2017). Global ionosphere maps based on GNSS, satellite altimetry, radio occultation and DORIS. *GPS Solutions, 21*(2), 639–650. https://doi.org/10.1007/s10291-016-0554-9

Cherniak, I., Zakharenkova, I., Braun, J., Wu, Q., Pedatella, N., Schreiner, W., Weiss, J.-P., & Hunt, D. (2021). Accuracy assessment of the quiet-time ionospheric F2 peak parameters as derived from COSMIC-2 multi-GNSS radio occultation measurements. *Journal of Space Weather and Space Climate, 11*, 18. https://doi.org/10.1051/swsc/2020080

Cherniak, I., Zakharenkova, I., Hunt, D., Weiss, J.-P., Braun, J., Vanhove, T., Sleziak-Sallee, M., & Pedatella, N. (2025). Evaluation of commercial GNSS radio occultation ionosphere and space weather data products using COSMIC-2. *GPS Solutions, 29*(3), 106. https://doi.org/10.1007/s10291-025-01874-0

Francis, S. H. (1974). A theory of medium-scale traveling ionospheric disturbances. *Journal of Geophysical Research, 79*(34), 5245–5260. https://doi.org/10.1029/JA079i034p05245

Gonzalez, W. D., Joselyn, J. A., Kamide, Y., Kroehl, H. W., Rostoker, G., Tsurutani, B. T., & Vasyliunas, V. M. (1994). What is a geomagnetic storm? *Journal of Geophysical Research. Space Physics, 99*(A4), 5771–5792. https://doi.org/10.1029/93JA02867

Han, H., Zhong, J., Hao, Y., Wang, N., Wan, X., Huang, F., Li, Q., Song, X., Chen, J., Wang, K., Tang, Y., Ou, Z., & Du, W. (2024). Effects of equatorial plasma bubbles on multi-GNSS signals: A case study over South China. *Remote Sensing (Basel), 16*(8), 1358. https://doi.org/10.3390/rs16081358

Hedin, A. E. (1987). MSIS-86 thermospheric model. *Journal of Geophysical Research. Space Physics, 92*(A5), 4649–4662. https://doi.org/10.1029/JA092iA05p04649

Hocke, K., & Schlegel, K. (1996). A review of atmospheric gravity waves and travelling ionospheric disturbances: 1982–1995. *Annales Geophysicae, 14*(9), 917–940. https://doi.org/10.1007/s00585-996-0917-6

Huang, F., Lei, J., Luan, X., Li, G., Wang, Y., Zhu, Y., Chen, J., Owolabi, C., & Dou, X. (2023). Dynamic processes associated with prominent ionospheric variations in a narrow longitudinal zone near the EIA crest region as revealed by ICON satellite and ground Beidou receiver observations over South Asia. *Journal of Geophysical Research: Space Physics, 128*(10), Article e2023JA031981. https://doi.org/10.1029/2023JA031981

Huang, F., Lei, J., Yue, X., Li, Z., Zhang, N., Cai, Y., Zhang, S., Wang, Y., Zhong, J., & Luan, X. (2025). Interplay of gravity waves and disturbance electric fields to the abnormal ionospheric variations during the 11 May 2024 superstorm. *AGU Advances, 6*(1), Article e2024AV001379. https://doi.org/10.1029/2024AV001379

Jakowski, N., Borries, C., & Wilken, V. (2012). Introducing a disturbance ionosphere index. *Radio Science, 47*(4), Article 2011RS004939. https://doi.org/10.1029/2011RS004939

Jakowski, N., & Hoque, M. M. (2019). Estimation of spatial gradients and temporal variations of the total electron content using ground-based GNSS measurements. *Space Weather, 17*(2), 339–356. https://doi.org/10.1029/2018SW002119

Klobuchar, J. (1987). Ionospheric time-delay algorithm for single-frequency GPS users. *IEEE Transactions on Aerospace and Electronic Systems, AES-23*(3), 325–331. https://doi.org/10.1109/taes.1987.310829

Li, G., Ning, B., Otsuka, Y., Abdu, M. A., Abadi, P., Liu, Z., Spogli, L., & Wan, W. (2021a). Challenges to equatorial plasma bubble and ionospheric scintillation short-term forecasting and future aspects in East and Southeast Asia. *Surveys in Geophysics, 42*(1), 201–238. https://doi.org/10.1007/s10712-020-09613-5

Li, W., & Jiang, Y. (2024). Equatorial plasma bubble model and integrity risk evaluation for ground based augmentation system in Hong Kong. *Satellite Navigation, 5*(1), 32. https://doi.org/10.1186/s43020-024-00154-5

Li, Z., Wang, N., Hernández-Pajares, M., Yuan, Y., Krankowski, A., Liu, A., Zha, J., García-Rigo, A., Roma-Dollase, D., Yang, H., Laurichesse, D., & Blot, A. (2020). IGS real-time service for global ionospheric total electron content modeling. *Journal of Geodesy, 94*(3), 32. https://doi.org/10.1007/s00190-020-01360-0

Li, Z., Wang, N., Liu, A., Yuan, Y., Wang, L., Hernández-Pajares, M., Krankowski, A., & Yuan, H. (2021b). Status of CAS global ionospheric maps after the maximum of solar cycle 24. *Satellite Navigation, 2*(1), 19. https://doi.org/10.1186/s43020-021-00050-2

Li, Z., Yuan, Y., Fan, L., Huo, X., & Hsu, H. (2014). Determination of the differential code bias for current BDS satellites. *IEEE Transactions on Geoscience and Remote Sensing, 52*(7), 3968–3979. https://doi.org/10.1109/TGRS.2013.2278545

Li, Z., Zhong, J., Hao, Y., Zhang, M., Niu, J., Wan, X., Huang, F., Han, H., Song, X., & Chen, J. (2023). Assessment of the orbital variations of GNSS GEO and IGSO satellites for monitoring ionospheric TEC. *GPS Solutions, 27*(2), 62. https://doi.org/10.1007/s10291-023-01403-x

Liu, L., Morton, Y. J., Cheng, P., Amores, A., Wright, C. J., & Hoffmann, L. (2023). Concentric traveling ionospheric disturbances (CTIDs) triggered by the 2022 Tonga volcanic eruption. *Journal of Geophysical Research-Space Physics, 128*(2), Article e2022JA030656. https://doi.org/10.1029/2022JA030656

Mannucci, A. J., Wilson, B. D., Yuan, D. N., Ho, C. H., Lindqwister, U. J., & Runge, T. F. (1998). A global mapping technique for GPS-derived ionospheric total electron content measurements. *Radio Science, 33*(3), 565–582. https://doi.org/10.1029/97RS02707

Nigussie, M., Jakowski, N., & Hoque, M. (2022). Characterization and climatological modeling of equatorial ionization anomaly (EIA) crest position. *Journal of Geophysical Research-Space Physics, 127*(12), Article e2022JA030798. https://doi.org/10.1029/2022JA030798

Nykiel, G., Ferreira, A., Günzkofer, F., Iochem, P., Tasnim, S., & Sato, H. (2024). Large-scale traveling ionospheric disturbances over the European sector during the geomagnetic storm on March 23–24, 2023: Energy deposition in the source regions and the propagation characteristics. *Journal of Geophysical Research-Space Physics*. https://doi.org/10.1029/2023ja032145

Pi, X., Mannucci, A. J., Lindqwister, U. J., & Ho, C. M. (1997). Monitoring of global ionospheric irregularities using the Worldwide GPS Network. *Geophysical Research Letters, 24*(18), 2283–2286. https://doi.org/10.1029/97GL02273

Rao, H., Chen, C., Meng, G., Liu, J., Sun, Y., Lin, K., Gao, Y., Rapoport, Y., Wang, F., Yisimayili, A., & Zhang, S. (2025). Relationship between TEC perturbations and Rayleigh waves associated with 2023 Turkey earthquake doublet. *Journal of Geophysical Research-Space Physics, 130*(1), Article e2024JA033267. https://doi.org/10.1029/2024JA033267

Sheng, Z., He, Y., Wang, S., Chang, S., Leng, H., Wang, J., Zhang, J., Wang, Y., Zhang, H., Sui, H., Song, Y., Wu, G., Guo, S., Chai, J., Feng, W., & Song, J. (2025). Dynamics, chemistry, and modeling studies in the aviation and aerospace transition zone. *Innovation (Cambridge)*. https://doi.org/10.1016/j.xinn.2025.101012

Sun, W., Li, G., Zhang, S., Zhao, B., Li, Y., Tariq, M. A., Zhao, X., Hu, L., Dai, G., Xie, H., Li, Y., Liu, J., Ning, B., & Liu, L. (2024). Complex ionospheric fluctuations over East and Southeast Asia during the May 2024 super geomagnetic storm. *Journal of Geophysical Research-Space Physics, 129*(12), Article e2024JA033096. https://doi.org/10.1029/2024JA033096

Tang, L., Zhang, F., Li, P., Deng, Y., & Chen, W. (2024). Effects of equatorial plasma bubble-induced ionospheric gradients on GNSS PPP-RTK. *GPS Solutions, 28*(3), 124. https://doi.org/10.1007/s10291-024-01664-0

Tsunoda, R. T., Livingston, R. C., McClure, J. P., & Hanson, W. B. (1982). Equatorial plasma bubbles: Vertically elongated wedges from the bottomside *F* layer. *Journal of Geophysical Research. Space Physics, 87*(A11), 9171–9180. https://doi.org/10.1029/JA087iA11p09171

Wang, B., Zhou, J., Wang, B., Cong, D., & Zhang, H. (2020). Influence of the GEO satellite orbit error fluctuation correction on the BDS WADS zone correction. *Satellite Navigation, 1*(1), 18. https://doi.org/10.1186/s43020-020-00020-0

Wang, N., Li, Y., Li, Z., Liu, A., & Liu, B. (2026). Determination of multi-GNSS differential code biases with satellite antenna phase center corrections. *GPS Solutions, 30*(1), 22. https://doi.org/10.1007/s10291-025-01983-w

Wang, N., Yuan, Y., Li, Z., Montenbruck, O., & Tan, B. (2016). Determination of differential code biases with multi-GNSS observations. *Journal of Geodesy, 90*(3), 209–228. https://doi.org/10.1007/s00190-015-0867-4

Wood, A. G., Alfonsi, L., Clausen, L. B. N., Jin, Y., Spogli, L., Urbář, J., Rawlings, J. T., Whittaker, I. C., Dorrian, G. D., Høeg, P., Kotova, D., Cesaroni, C., Cicone, A., Miedzik, J., Gierlach, E., Kochańska, P., Wojtkiewicz, P., Shahtahmassebi, G., & Miloch, W. J. (2022). Variability of ionospheric plasma: Results from the ESA Swarm Mission. *Space Science Reviews, 218*(6), 52. https://doi.org/10.1007/s11214-022-00916-0

Yang, Y., Mao, Y., & Sun, B. (2020). Basic performance and future developments of BeiDou global navigation satellite system. *Satellite Navigation, 1*(1), 1. https://doi.org/10.1186/s43020-019-0006-0

Zhai, C., Zhang, S., Yao, Y., Dong, W., Aa, E., Kong, J., Yue, D., Chen, Y., Peng, W., & Yu, T. (2025). Three-dimensional characterization of global ionospheric disturbances during the 15 January 2022 Tonga volcanic eruption. *Geophysical Research Letters, 52*(2), Article e2024GL113129. https://doi.org/10.1029/2024GL113129

Zhang, Z., Wang, N., Liu, A., Li, Z., Li, A., Wang, L., & Zhang, Y. (2025). Assessing 1-second ROTI for ionospheric perturbation monitoring using real-time multi-GNSS data in China. *Space Weather, 23*(2), Article e2024SW004187. https://doi.org/10.1029/2024SW004187

Zhong, J., Han, H., Hao, Y., Wan, X., Huang, F., Li, Q., Song, X., Chen, J., & Lei, J. (2023). Accurate estimation of height and zonal drift velocity of ionospheric irregularities using two pairs of receivers and BeiDou geostationary satellites. *IEEE Transactions on Geoscience and Remote Sensing, 61*, 1–10. https://doi.org/10.1109/TGRS.2023.3326441

Zhong, J., Lei, J., Dou, X., & Yue, X. (2016a). Assessment of vertical TEC mapping functions for space-based GNSS observations. *GPS Solutions, 20*(3), 353–362. https://doi.org/10.1007/s10291-015-0444-6

Zhong, J., Lei, J., Dou, X., & Yue, X. (2016b). Is the long-term variation of the estimated GPS differential code biases associated with ionospheric variability? *GPS Solutions, 20*(3), 313–319. https://doi.org/10.1007/s10291-015-0437-5

Zhong, J., Lei, J., Yue, X., Luan, X., & Dou, X. (2019). Middle-latitudinal band structure observed in the nighttime ionosphere. *Journal of Geophysical Research. Space Physics, 124*(7), 5857–5873. https://doi.org/10.1029/2018JA026059

Publisher's Note